Nano Research
2021, 14(4): 1149–1155

ISSN 1998-0124 CN 11-5974/O4
https://doi.org/10.1007/s12274-020-3164-3

Research Article

Heterogeneous lamellar-edged Fe-Ni(OH)$_2$/Ni$_3$S$_2$ nanoarray for efficient and stable seawater oxidation

Baihua Cui[1,2,3], Zheng Hu[4], Chang Liu[3], Siliang Liu[3], Fangshuai Chen[3], Shi Hu[4], Jinfeng Zhang[3], Wei Zhou[4], Yida Deng[3], Zhenbo Qin[3], Zhong Wu[3] (✉), Yanan Chen[3] (✉), Lifeng Cui[1] (✉), and Wenbin Hu[2,3] (✉)

[1] *School of Materials Science and Engineering, Dongguan University of Technology, Dongguan 523808, China*
[2] *Joint School of National University of Singapore and Tianjin University, International Campus of Tianjin University, Fuzhou 350207, China*
[3] *School of Materials Science and Engineering, Tianjin University, Tianjin 300372, China*
[4] *School of Science, Tianjin University, Tianjin 300072, China*

Received: 25 August 2020 / **Revised:** 1 October 2020 / **Accepted:** 8 October 2020

ABSTRACT

Development of efficient non-precious catalysts for seawater electrolysis is of great significance but challenging due to the sluggish kinetics of oxygen evolution reaction (OER) and the impairment of chlorine electrochemistry at anode. Herein, we report a heterostructure of Ni_3S_2 nanoarray with secondary Fe-Ni(OH)$_2$ lamellar edges that exposes abundant active sites towards seawater oxidation. The resultant Fe-Ni(OH)$_2$/Ni_3S_2 nanoarray works directly as a free-standing anodic electrode in alkaline artificial seawater. It only requires an overpotential of 269 mV to afford a current density of 10 mA·cm^{-2} and the Tafel slope is as low as 46 mV·dec^{-1}. The 27-hour chronopotentiometry operated at high current density of 100 mA·cm^{-2} shows negligible deterioration, suggesting good stability of the Fe-Ni(OH)$_2$/Ni_3S_2@NF electrode. Faraday efficiency for oxygen evolution is up to ~ 95%, revealing decent selectivity of the catalyst in saline water. Such desirable catalytic performance could be benefitted from the introduction of Fe activator and the heterostructure that offers massive active and selective sites. The density functional theory (DFT) calculations indicate that the OER has lower theoretical overpotential than Cl_2 evolution reaction in Fe sites, which is contrary to that of Ni sites. The experimental and theoretical study provides a strong support for the rational design of high-performance Fe-based electrodes for industrial seawater electrolysis.

KEYWORDS

lamellar edges, Fe-Ni(OH)$_2$/Ni_3S_2, seawater oxidation, chlorine electrochemistry, electrocatalysis

1 Introduction

Production of hydrogen via water electrolysis is regarded as a sustainable energy conversion process that appeals to extensive attention around the world [1–4]. Currently, most of the electrocatalytic systems are operated in electrolytes with freshwater at different pH [5–9]. Limited by reserves and distribution on earth, freshwater is not a good choice that suitable for all regions. The hydrogen and oxygen produced from seawater splitting have tremendous advantages over freshwater, due to the huge storage of salty water on earth [10]. However, practical seawater electrolysis still faces various challenges to overcome, such as unsatisfactory oxygen evolution reaction (OER) kinetics and impairment of chlorine electrochemistry [11–13]. Compared to two-electron involved hydrogen evolution reaction (HER), four-electron participated OER is such a sluggish process that considered as a bottleneck of water electrolysis [14, 15]. Also, the chlorine competition reaction and corrosion effect resulted from high concentration of Cl^- are major issues for seawater electrolysis [16, 17]. Therefore, achieving overall seawater electrolysis with high efficiency and stability is critical but challenging.

The potential difference between chlorine evolution reaction (CER) and OER in the Pourbaix diagram maximized to ~ 0.48 V when pH > 7.5, suggesting the superiority of OER in thermodynamics at high pH media [18]. Note that to avoid CER competition requires operating OER at a limited potential range, thereby how to achieve high current with low overpotential becomes a new goal. The potential for further improvements in these fields are less-investigated and the activity and selectivity of the studied catalysts remain unsatisfactory due to less active sites [19–21]. In addition, most previously employed materials could inevitably suffer from corrosion by aggressive chlorinated compound in seawater [22–24]. Recent researches on *in-situ* generated species during OER have been proved helpful for anti-corrosion from aggressive Cl^-. Kuang et al. [17] reported that the polyatomic sulfate-rich passivation layers were *in-situ* generated from electrode during OER and afforded excellent corrosion resistance of the anode by chloride repelling. Yu et al. [25] claimed that the improved resistance to Cl^- corrosion in seawater was derived from the *in situ* evolved amorphous layers of oxide/oxy(hydroxide). However, some electrocatalysts, despite showing decent stability, have yet to demonstrate a sufficient catalytic capability for fast electrolysis at low overpotential [26–28]. To date, the explorations of the high-performance catalysts with abundant active sites

Address correspondence to Zhong Wu, wuzhong2319@163.com; Yanan Chen, yananchen@tju.edu.cn; Lifeng Cui, lcui@usst.edu.cn; Wenbin Hu, wbhu@tju.edu.cn

and corrosion resistance in saline electrolyte just start-up and have great potential.

Herein, we report a heterostructured Fe-Ni(OH)$_2$/Ni$_3$S$_2$@NF electrode with lamellar edges that exhibits numerous active sites towards high-performance seawater oxidation. Benefitted from the introduction of Fe activator and integration of the active Fe-Ni(OH)$_2$ on Ni$_3$S$_2$ nanoarray, the heterostructure exhibits superior electrocatalytic performance for alkaline seawater oxidation. The lamellar-edged Fe-Ni(OH)$_2$/Ni$_3$S$_2$ only needs a low overpotential of 269 mV to reach 10 mA·cm^{-2} and the Tafel slope is 46 mV·dec^{-1}. Also, it maintained a good durability at 100 mA·cm^{-2} steadily for 27-hour continuous oxygen production. The whole Faraday efficiency of ~ 95% suggested great selectivity of the synthesized catalyst in chlorine-contained electrolyte. The preferable catalytic sites for OER and CER are investigated in artificial seawater system by density functional theory (DFT) calculations. The results indicate that the Fe species play as active sites in catalyzing OER with low overpotential while Ni can be potential catalytic sites for CER. These may offer clues on designing practical Fe-based electrodes with good performance for industrial seawater electrolysis.

2 Experiments

2.1 Materials preparation

Synthesis of Fe-Ni(OH)$_2$/Ni$_3$S$_2$ nanoarray precursor on Ni foam. A piece of Ni foam (NF, typically 2 cm × 3 cm × 0.15 cm) was pretreated by 3 M HCl, ethanol, and deionized water under sonication. 2.2 mg thiourea was dissolved in 20 mL of deionized water. Then, the homogeneous solution together with NF was transferred to 50-mL Teflon-lined stainless autoclave and heated at 150 ℃ for 5 h in an oven. The product was taken out after cooling down to room temperature and washed with deionized water and ethanol for further dried at ambient temperature. Electrodeposition was applied to achieve Fe doping on nanoarray in a three-electrode cell by directly using the product Ni$_3$S$_2$@NF as the working electrode, Pt foil and saturated calomel electrode (SCE) as the counter electrode and reference electrode, respectively. The electrodeposition was conducted in the solution (50 mL) containing 0.001 M Fe(NO$_3$)$_3$, 0.0025 M ammonium oxalate and 0.001 M NaCl at −1 mA for different time [29]. The fabricated Fe-Ni(OH)$_2$/Ni$_3$S$_2$ was taken out of the cell immediately and washed by deionized water to remove residual electrolyte and dried in the air naturally for further use. The preparation of Ni(OH)$_2$@NF and Fe-Ni(OH)$_2$@NF were same with above procedure except replacement of thiourea with urea.

2.2 Materials characterization

The morphology was investigated using JEOL JSM-7800F scanning electron microscopy (SEM), JEOL JEM-2100F and JEOL JEM-ARM200F transmission electron microscopy (TEM, 200 kV). The X-ray photoelectron spectroscopy (XPS) results were collected from Escalab 250Xi Thermo Fisher Scientific spectrometer (X-ray source for excitation: Al Kα radiation). The oxygen evolved from OER was measured by Agilent-6890 gas chromatograph (thermal conductivity detector, TCD) for Faraday efficiency analysis. The Raman spectrum was collected on HORIBA Jobin Yvon LabRAM HR Evolution Raman microscope (532-nm laser).

2.3 Electrochemical measurements

Electrochemical tests were performed in a CHI760E electrochemical workstation (Chenhua, China) via a three-electrode system. The Hg/HgO electrode and Pt foil were used as reference and counter electrodes, respectively. The as-synthesized free-standing sample was used directly as working electrode. The cyclic voltammetry (CV) scans were performed at a scan rate of 5 mV·s^{-1} in 1 M KOH+0.5 M NaCl solution. Electrochemical impedance spectroscopy (EIS) was conducted at an overpotential of 300 mV where the frequency ranges from 0.1 to 10^4 Hz. The CV curves here were compensated with *iR* (95%). The stability of electrocatalyst was evaluated by long-term electrolysis at 100 mA·cm^{-2} for 27 h. The experimental setup for Faraday efficiency was a sealed H-type cell with 1 M KOH + 0.5 M NaCl solution, where Pt plate (1 cm × 1 cm) and Ag/AgCl were used as counter and reference electrodes, respectively. After many cycles of CV test for a stable catalytic performance, the electrolysis was carried out on a CS-150H workstation at current density of 20 mA·cm^{-2}, maintaining continuous oxygen production for 10 h at room temperature. Meanwhile, high-purity Ar gas as carrier was purged into anodic compartment at a flow rate of 20 sccm to carry oxygen to gas chromatograph (Agilent-6890) equipped with TCD for quantification. The Faraday efficiency (FE) of oxygen form OER in the reaction system was calculated by following equation [30]

$$\mathrm{FE} = \frac{znF}{Q} = \frac{zF}{Q} \cdot \frac{PV\alpha}{RT}$$

where z represents the number of electrons transfer per O_2 molecule, the Faraday constant F is 96,500 C·mol^{-1}, the temperature T in this system is 298 K, Q is the charge obtained under the corresponding current, V is the volume of the gas in the sealed system, and α is the gas volume fraction obtained by gas chromatography (GC).

3 Results and discussion

3.1 Physical characterization

The lamellar-edged Fe-Ni(OH)$_2$/Ni$_3$S$_2$ nanoarray grown on Ni foam was synthesized by the hydrothermal method together with electrochemical deposition, as schematically demonstrated in Scheme 1. We synthesized Ni$_3$S$_2$ nanoarray according to the previous report [31]. The characterization with SEM and X-ray diffraction (XRD) were conducted for precursor, revealing nickel sulfide precursor with smooth surface grown on Ni foam uniformly (Figs. S1 and S2 in the Electronic Supplementary Material (ESM)). During the electrodeposition process, NO_3^- ions were reduced to generate OH^- (Eq. (1)) [32]. Ni and Fe then reacted with surrounding OH^- to form ordered bimetallic hydroxide at the edges of Ni$_3$S$_2$ nanoarray according to Eq. (2)

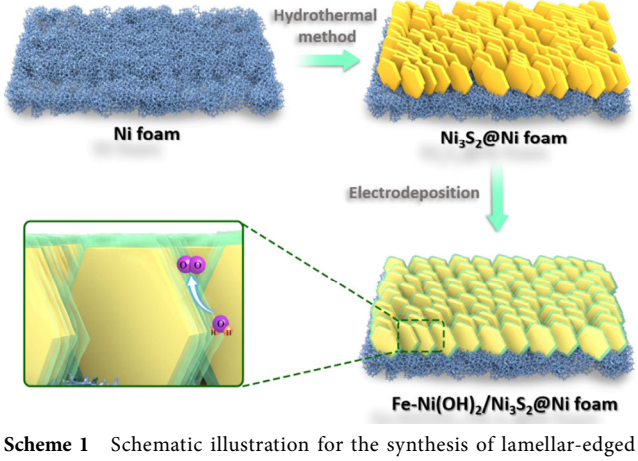

Scheme 1 Schematic illustration for the synthesis of lamellar-edged Fe-Ni(OH)$_2$/Ni$_3$S$_2$ nanoarray.

$$NO_3^- + 7H_2O + 8e^- \rightarrow NH_4^+ + 10OH^- \quad (1)$$

$$Ni^{2+} + Fe^{3+} + 2OH^- \rightarrow Fe\text{-}Ni(OH)_2 \quad (2)$$

The lamellar-edged nanoarray perpendicularly grew on Ni foam skeleton and interlaced with each other (Figs. 1(a)–1(c)). The orderly microstructure offers more open space to effectively favor the permeation of electrolyte and diffusion of gas production. The thin layers with clear interspace were observed at the edge of those nanoplates forming a lamellar lace (Figs. 1(d) and 1(e)). The hierarchical structure exposes more surface area that provide a great number of active sites for reaction species accelerating the overall reaction rate. The low contrast area of the selected edge part (Fig. 1(f)) exhibited a thin layer feature with slight amorphization, such structural traits were supposed to possess abundant surface defects [33, 34]. The fast Fourier transform (FFT) pattern (inset of Fig. 1(f)) showed (110) and (100) facets diffraction of $Ni(OH)_2$ (JCPDS No. 73-1520). The energy-dispersive X-ray spectroscopy (EDX) elemental mapping (Fig. S3 in the ESM) presented the distribution of Ni, O, S, and Fe elements over the nanoplate. The heterogeneous Fe-$Ni(OH)_2$/Ni_3S_2 nanoarray with lamellar edges was successfully synthesized via a two-step wet chemical method.

The structural information of Fe-$Ni(OH)_2$/Ni_3S_2 was also characterized by the Raman spectrum (Fig. 2(a)). It possessed

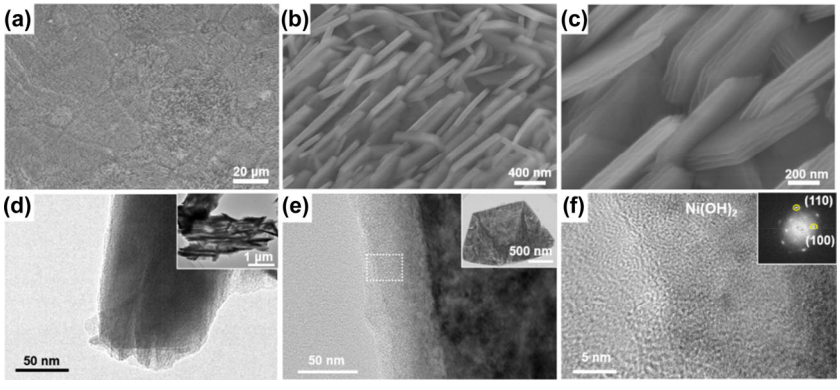

Figure 1 (a)–(c) SEM images of Fe-$Ni(OH)_2$/Ni_3S_2 nanoarray peeled from Ni foam. (d) TEM images of the lateral edge at a vertical plate (inset: vertically arranged nanoarray). (e) TEM images of the edge at the plate (inset: horizontal plane of nanoplate). (f) HRTEM images of the selected area in (e) and corresponding FFT pattern as an inset.

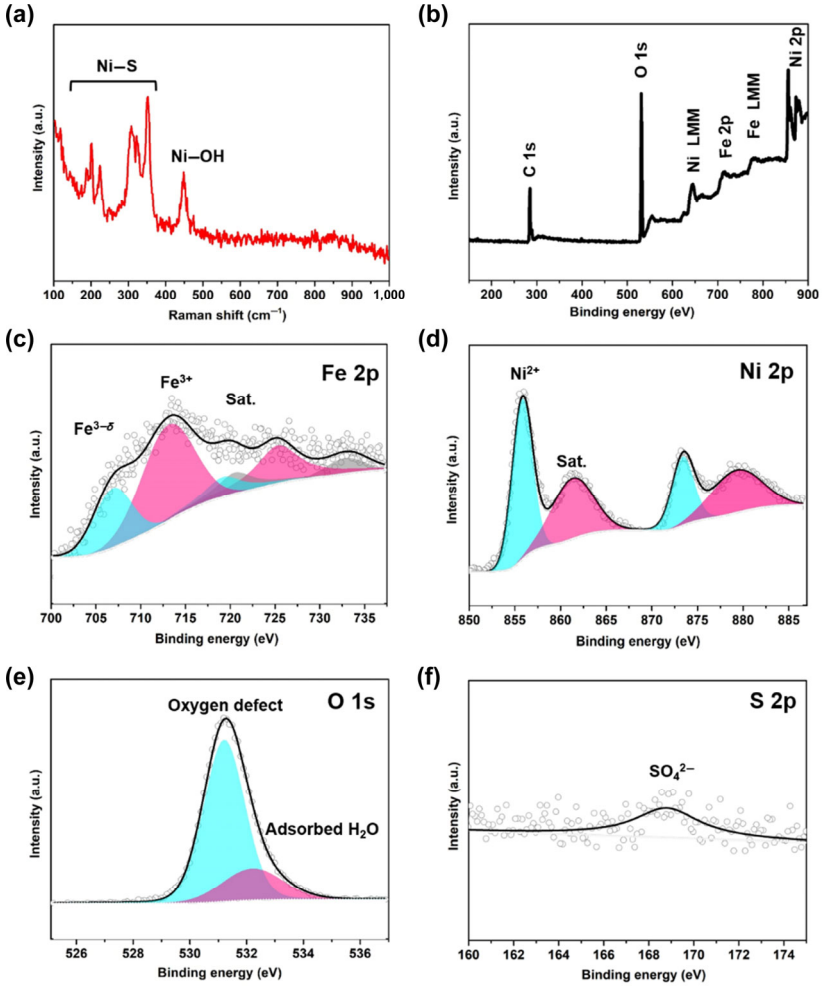

Figure 2 (a) Raman spectrum and (b) XPS survey spectra of Fe-$Ni(OH)_2$/Ni_3S_2@NF, as well as corresponding high-resolution XPS spectra of (c) Fe 2p and (d) Ni 2p (e) O1s (f) S 2p.

the typical Raman vibration peaks of Ni–S at 188, 198, 221, 303, 322, and 349 cm^{-1} from Ni_3S_2 [35]. The evident peak at ~ 450 cm^{-1} can be assigned to Ni–OH vibration in Fe doped $Ni(OH)_2$ layer [36]. For more insight into the elemental composition and chemical state of the as-prepared sample, XPS measurement was employed. The XPS survey spectrum (Fig. 2(b)) revealed the existence of Ni, Fe, O, and S atoms on the surface of Fe-$Ni(OH)_2/Ni_3S_2$. In the Fe 2p spectrum (Fig. 2(c)), the two peaks at binding energies of 713.1 and 725.2 eV can be consigned to Fe^{3+} 3/2 and Fe^{3+} 1/2, respectively, with their satellite peaks at 720.5 and 732.8 eV (denoted as Sat.) [37]. The peaks located at 706.9 and 719.2 eV could be attributed to low oxidation state $Fe^{3-\delta}$, revealing the coexistence of Fe species with different valence [38]. The Ni 2p spectra included (Fig. 2(d)) two spin-orbit peaks at 855.9 and 873.5 eV, namely Ni^{2+} $2p_{3/2}$ and $2p_{1/2}$, accompanied by two shake-up satellites at 861.4 and 879.4 eV [39]. The peaks centered at 531.3 and 532.2 eV in the O 1s curve (Fig. 2(e)) are usually ascribed to oxygen defect and adsorbed H_2O, respectively [40]. The XPS curve of S 2p was one broad bump situated at 168.8 eV (Fig. 3(f)), belonging to SO_4^{2-} probably generated from slightly surface oxidation [41]. Those results gave detailed information of Fe doped $Ni(OH)_2$ bimetallic hydroxide lamellar structure that grown on Ni_3S_2 nanoplates.

3.2 Electrocatalytic performance

To investigate the electrocatalytic capability of Fe-$Ni(OH)_2/Ni_3S_2$@NF, we performed electrochemical measurements in alkaline seawater. CV curves in Fig. 3(a) compared the performance of Fe-$Ni(OH)_2/Ni_3S_2$@NF catalyst toward OER together with Ni foam and Ni_3S_2@NF. As- fabricated catalyst only needs as low overpotential as 269 mV to reach a current density of 10 $mA·cm^{-2}$, while precursor Ni_3S_2@NF and Ni foam required higher overpotential of 370 mV to reach the same level. Such electrocatalytic outcomes were superior than numerous previous studies on seawater splitting (Table S1 in the ESM). Besides, the performance of Fe-$Ni(OH)_2/Ni_3S_2$@NF with different deposited time were evaluated and the results indicated that neither shorter nor longer time than 30 s led to boosted activity (Fig. S4 in the ESM). The appropriate Fe content is necessary for optimal catalytic results [42– 44]. It is noted that Fe-$Ni(OH)_2/Ni_3S_2$@NF featured a different Ni^{2+} oxidation peak and superior OER activity than Ni_3S_2@NF, indicating the introduction of Fe involved into OER and modulate the Ni sites to some extent [45, 46]. Meanwhile, the Tafel slope of Fe-$Ni(OH)_2/Ni_3S_2$@NF in Fig. 3(b) is only 46 $mV·dec^{-1}$ that considerably smaller than that of Ni_3S_2@NF (112 $mV·dec^{-1}$) and bare Ni Foam (about 120 $mV·dec^{-1}$). The small Tafel slope value means the catalyst can afford a large current density at low reaction overpotential driven by rapid kinetics [47]. Such good performance could be benifitted from the structural merits of lamellar-edged nanoplate as mentioned above. EIS was performed to investigate the charge transfer resistance (R_{ct}) of those samples (Fig. 3(c)). The smaller R_{ct} (~ 1.7 Ω) of Fe-$Ni(OH)_2/Ni_3S_2$@NF than that of bare Ni foam and Ni_3S_2@NF suggested faster electron transfer process of OER at Fe-$Ni(OH)_2/Ni_3S_2$@NF electrode [48]. The micro-interface in heterogeneous structure is likely to favor the charge transfer in the Faraday process.

The chronopotentiometry was adopted to evaluate the durability of Fe-$Ni(OH)_2/Ni_3S_2$@NF (Fig. 3(d)) and displayed decent stability at 100 $mA·cm^{-2}$ for 27 h with negligible decay. The catalyst after OER tests was studied to examine the structural robustness in a highly oxidative and corrosive environment. The SEM (Fig. S5 in the ESM) images showed intact and uniform nanoarray on Ni foam skeleton, verifying the good resistance to corrosion during OER. The contrast experiment to evaluate the performance of Fe-$Ni(OH)_2$@NF was conducted to investigate the important role of Ni_3S_2 in anti-corrosion. Although Fe-$Ni(OH)_2$@NF showed comparable activity with Fe-$Ni(OH)_2/Ni_3S_2$@NF, the evident degradation was observed in potentiostatic test (Fig. S6 in the ESM). With study on structure of tested catalysts, remarkable morphology change in Fe-$Ni(OH)_2$@Ni foam was found (Fig. S7 in the ESM) and

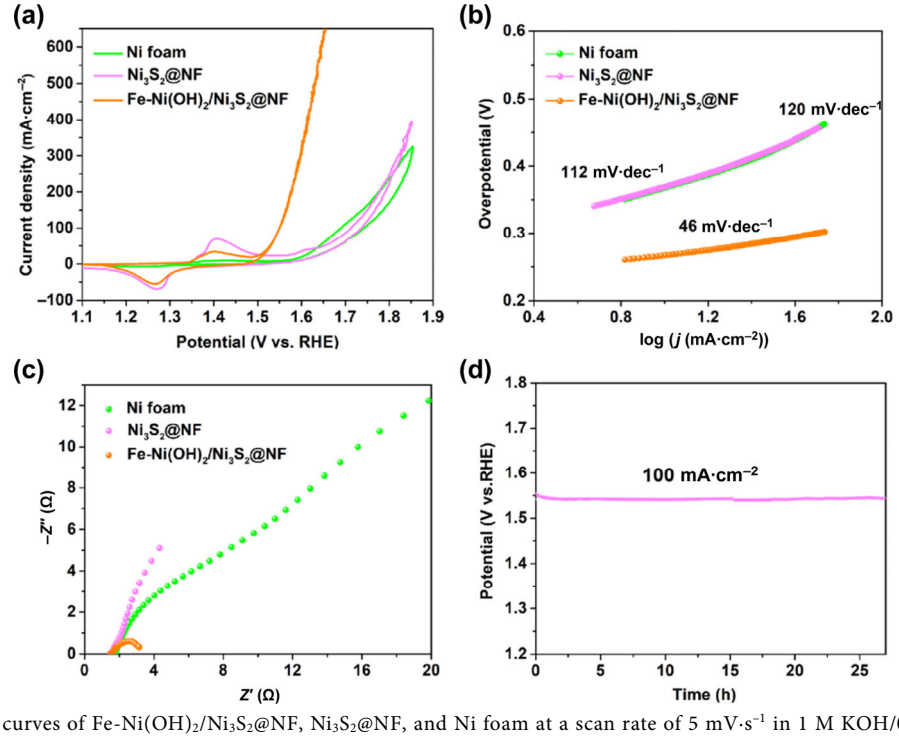

Figure 3 (a) The CV curves of Fe-$Ni(OH)_2/Ni_3S_2$@NF, Ni_3S_2@NF, and Ni foam at a scan rate of 5 $mV·s^{-1}$ in 1 M KOH/0.5 NaCl, together with corresponding Tafel plots (b). (c) The Nyquist plots of various catalysts at η = 300 mV. (d) Time-dependent current density curve of Fe-$Ni(OH)_2/Ni_3S_2$@NF under 100 $mA·cm^{-2}$ for 27 h.

that may explain the deterioration in stability. Only small surface change took place on Fe-Ni(OH)$_2$/Ni$_3$S$_2$ observed from TEM images Fig. S8(a) and S8(b) in the ESM. The high resolution TEM (HRTEM) image (Fig. S8(c) in the ESM) displayed crystal planes of NiOOH with the interplanar distance of 0.20 and 0.24 nm, which is consistent with the appearance of redox peak $Ni^{2+} \rightarrow Ni^{3+}$ in CV curves during OER [49]. The NiOOH is commonly detected from tested sample at OER and regarded as active species for the water oxidation [45, 49]. The corresponding EDX elemental mappings (Fig. S8(d) in the ESM) gave the information of Ni, O, S, and Fe elements distributed over the sample. Apart from Ni-S and Ni-OH peaks in Raman curves (Fig. S9 in the ESM), the broad peak from 450 to 550 cm^{-1} can be attributed to Ni(III)-O from NiOOH after OER test [45, 50]. The analysis indicated such heterostructure Fe-Ni(OH)$_2$/Ni$_3$S$_2$@NF electrode is highly effective and structurally stable in continuous OER operation at salty electrolyte.

Beyond activity and stability, another critical criterion for evaluation of catalysts' efficiency in seawater oxidation is selectivity. The performance of OER tests performed in alkaline freshwater was compared with that in simulated seawater (Fig. 4(a)). The closer outcomes on three key indicators (R_{ct}, Tafel slope, and overpotential at 10 mA·cm^{-2}) proved that the heterostructure has a good OER activity even in a high-salinity solution. Furthermore, Faraday efficiency of O_2 production in simulated seawater was measured quantitatively using gas chromatography to assess the selectivity of as-prepared catalyst (Fig. 4(b)). An average 95% Faradaic efficiency towards OER suggested chlorine competitive reaction was suppressed. Therefore, our lamellar-edged heterogeneous electrode possesses desirable electrocatalytic properties in terms of activity, stability, and selectivity, manifesting it as a practical candidate for seawater electrolysis (Fig. 4(c)).

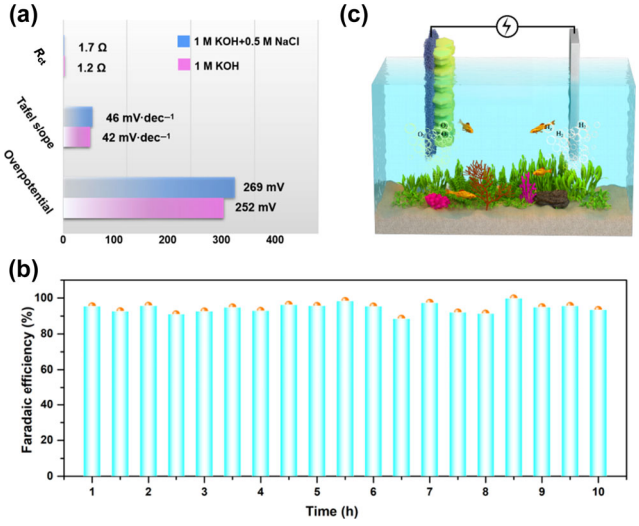

Figure 4 (a) The comparison of the electrocatalytic performance of Fe-Ni(OH)$_2$/Ni$_3$S$_2$@NF in alkaline freshwater (1 M KOH) and seawater (1 M KOH+0.5 M NaCl). (b) Faraday efficiency of oxygen production from OER in alkaline seawater. (c) Typical electrolyzer for seawater electrolysis.

3.3 Theoretical calculations

Furthermore, DFT calculations were performed as an attempt to find possible active sites for OER and CER at Fe-Ni(OH)$_2$/Ni$_3$S$_2$@NF anode. The (100) and (110) facets of Fe-Ni(OH)$_2$ were used for building the catalysis slab model (Fig. 5(a))

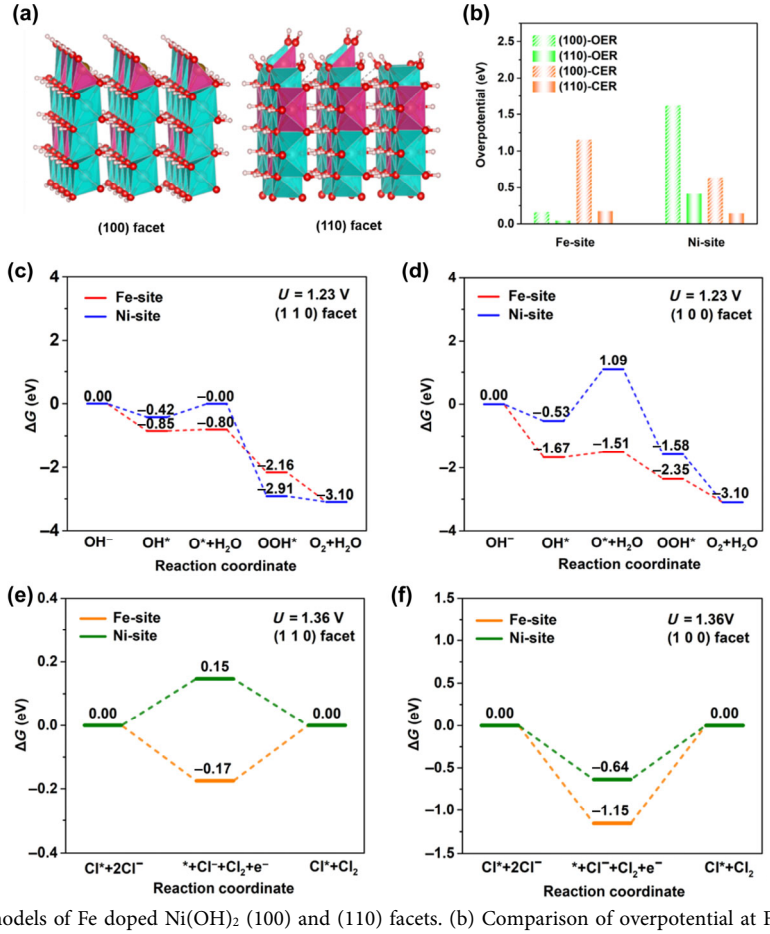

Figure 5 (a) The structural models of Fe doped Ni(OH)$_2$ (100) and (110) facets. (b) Comparison of overpotential at Fe or Ni-site in (110) and (100) facets for CER and OER. DFT calculation of the Gibbs free energy changes, the OER catalyzed at (110) facet (c) and (100) facet (d). The CER catalyzed at (110) facet (e) and (100) facet (f).

according to TEM results. Figure S10 in the ESM exhibited optimized model structures of corresponding intermediates adsorbed at different surface sites. A well-accepted OER mechanism was employed to study the kinetics through DFT calculation in Figs. 5(c) and 5(d) [51]. Thermodynamic analyses suggested that the transformation from OH* to O* is an endothermic process with the highest barrier in both (100) and (110) facets, which means the rate-determining step (RDS) here for OER lies in the formation of *O. Obviously, Fe-site had lower thermodynamic barrier (ΔG) than Ni-site at both of two facets, indicating the Fe-site is more active for OER. As for the theoretical overpotential (η_{OER}) at two different facets, Fe in (110) facet had a smaller value than that in (100) facet (Fig. 5(b)). Meanwhile, the CER processes were studied via the Volmer-Heyrovsky mechanism in Figs. 5(e) and 5(f), where Heyrovsky step was identified as the RDS in CER based on previous study [52]. For both (110) and (100) facets, the calculated η_{CER} in Ni site was lower than that of Fe, implying the possible catalytic sites for CER is Ni-site (Fig. 5(b)). Similar to OER, the (110) facet gave lower theoretical η_{CER} in Ni-site than (100) facet. Comparing the overpotential of Fe-site in OER and Ni-site in CER at the seawater system, we discovered the former gave a lower value. These results suggested that OER is a more favorable and dominant anodic process than CER on the Fe-site of as-prepared electrode in the seawater electrolysis system.

4 Conclusion

In summary, we constructed a heterogeneous architecture of lamellar-edged Fe-Ni(OH)$_2$/Ni$_3$S$_2$ nanoarray as a highly efficient catalyst for seawater oxidation. The nano/micro sheet-on-plate structure and the hybrid composition of Fe-Ni(OH)$_2$/Ni$_3$S$_2$ were investigated by systematic characterizations. The lamellar edges and intimate contact between Fe-Ni(OH)$_2$ and Ni$_3$S$_2$ provided large exposed area, facilitating the electron/mass transfer and prompting gas release from the surface. DFT calculations revealed the Fe species, rather than Ni, in lamellar edges act as highly active and selective sites for OER in artificial seawater. As a result, the superior electrocatalytic performance was achieved by the design of hierarchical electrode and introduction of OER-preferable species with fast kinetics, long-term stability, and good selectivity in seawater oxidation. This work offers an avenue to the rational design of cost-efficient and high-performance electrocatalysts for practical seawater electrolysis.

Acknowledgements

We acknowledge the financial support from the National Natural Science Foundation of China (No. 91963113).

Electronic Supplementary Material: Supplementary material (SEM/TEM images, XRD patterns, Raman spectra, electrochemical results from CV and potentiostatic test, table on comparison of electrocatalytic performance and simulation details) is available in the online version of this article at https://doi.org/10.1007/s12274-020-3164-3.

References

[1] Gong, M.; Dai, H. J. A mini review of NiFe-based materials as highly active oxygen evolution reaction electrocatalysts. *Nano Res*. **2015**, *8*, 23–39.

[2] Liu, J. L.; Zhu, D. D.; Ling, T.; Vasileff, A.; Qiao, S. Z. S-NiFe$_2$O$_4$ ultra-small nanoparticle built nanosheets for efficient water splitting in alkaline and neutral pH. *Nano Energy* **2017**, *40*, 264–273.

[3] Fu, L. H.; Li, Y. B.; Yao, N.; Yang, F. L.; Cheng, G. Z.; Luo, W. IrMo nanocatalysts for efficient alkaline hydrogen electrocatalysis. *ACS Catal*. **2020**, *10*, 7322–7327.

[4] Dou, S. M.; Xu, J.; Cui, X. Y.; Liu, W. D.; Zhang, Z. C.; Deng, Y. D.; Hu, W. B.; Chen, Y. N. High-temperature shock enabled nanomanufacturing for energy-related applications. *Adv. Energy Mater*. **2020**, *10*, 2001331.

[5] Xie, X. H.; Song, M.; Wang, L. G; Engelhard, M. H.; Luo, L. L.; Miller, A.; Zhang, Y. Y.; Du, L.; Pan, H. L.; Nie, Z. M. et al. Electrocatalytic hydrogen evolution in neutral pH solutions: Dual-phase synergy. *ACS Catal*. **2019**, *9*, 8712–8718.

[6] Fan, C.; Jiang, X.; Chen, J. Y.; Wang, X.; Qian, S. Y.; Zhao, C. Z.; Ding, L. F.; Sun, D. M.; Tang, Y. W. Low-load Pt nanoclusters anchored on graphene hollow spheres for efficient hydrogen evolution. *Small Struct*., in press, DOI: 10.1002/sstr.202000017.

[7] Reier, T.; Nong, H. N.; Teschner, D.; Schlögl, R.; Strasser, P. Electrocatalytic oxygen evolution reaction in acidic environments-reaction mechanisms and catalysts. *Adv. Energy Mater*. **2017**, *7*, 1601275.

[8] Wu, H.; Lu, Q.; Zhang, J. F.; Wang, J. J.; Han, X. P.; Zhao, N. Q.; Hu, W. B.; Li, J. J.; Chen, Y. N.; Deng, Y. D. Thermal shock-activated spontaneous growing of nanosheets for overall water splitting. *Nano-Micro Lett*. **2020**, *12*, 162.

[9] Zhang, J.; Chen, Z. L.; Liu, C.; Zhao, J.; Liu, S. L.; Rao, D. W.; Nie, A. M.; Chen, Y. N.; Deng, Y. D.; Hu, W. B. Hierarchical iridium-based multimetallic alloy with double-core-shell architecture for efficient overall water splitting. *Sci. China Mater*. **2020**, *63*, 249–257.

[10] Dresp, S.; Dionigi, F.; Klingenhof, M.; Strasser. P. Direct electrolytic splitting of seawater: Opportunities and challenges. *ACS Energy Lett*. **2019**, *4*, 933–942.

[11] Yu, L.; Wu, L. B.; McElhenny, B.; Song, S. W.; Luo, D.; Zhang, F. H.; Yu, Y.; Chen, S.; Ren, Z. F. Ultrafast room-temperature synthesis of porous S-doped Ni/Fe (oxy)hydroxide electrodes for oxygen evolution catalysis in seawater splitting. *Energy Environ. Sci*., in press, DOI: 10.1039/D0EE00921K.

[12] Dresp, S.; Thanh, T. N.; Klingenhof, M.; Brückner, S.; Hauke, P.; Strasser, P. Efficient direct seawater electrolysers using selective alkaline NiFe-LDH as OER catalyst in asymmetric electrolyte feeds. *Energy Environ. Sci*. **2020**, *13*, 1725–1729.

[13] Keane, T. P.; Nocera, D. G. Selective production of oxygen from seawater by oxidic metallate catalysts. *ACS Omega* **2019**, *4*, 12860–12864.

[14] Chen, Y. N.; Xu, S. M.; Zhu, S. Z.; Jacob, R. J.; Pastel, G.; Wang, Y. B.; Li, Y. J.; Dai, J. Q.; Chen, F. J.; Xie, H. et al. Millisecond synthesis of CoS nanoparticles for highly efficient overall water splitting. *Nano Res*. **2019**, *12*, 2259–2267.

[15] Hao, C. Y.; Wu, Y.; An, Y. J.; Cui, B. H.; Lin, J. N.; Li, X. N.; Wang, D. H.; Jiang, M. H.; Cheng, Z. X.; Hu, S. Interface-coupling of CoFe-LDH on MXene as high-performance oxygen evolution catalyst. *Mater. Today Energy* **2019**, *12*, 453–462.

[16] Tong, W. M.; Forster, M.; Dionigi, F.; Dresp, S.; Erami, R. S.; Strasser, P.; Cowan, A. J.; Farràs, P. Electrolysis of low-grade and saline surface water. *Nat. Energy* **2020**, *5*, 367–377.

[17] Kuang, Y.; Kenney, M. J.; Meng, Y. T.; Hung, W. H.; Liu, Y. J.; Huang, J. E.; Prasanna, R.; Li, P. S.; Li, Y. P.; Wang, L. et al. Solar-driven, highly sustained splitting of seawater into hydrogen and oxygen fuels. *Proc. Natl. Acad. Sci. USA* **2019**, *116*, 6624–6629.

[18] Dionigi, F.; Reier, T.; Pawolek, Z.; Gliech, M.; Strasser, P. Design criteria, operating conditions, and nickel-iron hydroxide catalyst materials for selective seawater electrolysis. *ChemSusChem* **2016**, *9*, 962–972.

[19] Okada, T.; Abe, H.; Murakami, A.; Shimizu, T.; Fujii, K.; Wakabayashi, T.; Nakayama, M. A bilayer structure composed of Mg|Co-MnO$_2$ deposited on a Co(OH)$_2$ film to realize selective oxygen evolution from chloride-containing water. *Langmuir* **2020**, *36*, 5227–5235.

[20] Vos, J. G.; Wezendonk, T. A.; Jeremiasse, A. W.; Koper, M. T. M. MnO$_x$/IrO$_x$ as selective oxygen evolution electrocatalyst in acidic chloride solution. *J. Am. Chem. Soc*. **2018**, *140*, 10270–10281.

[21] Zhao, Y. Q.; Jin, B.; Zheng, Y.; Jin, H. Y.; Jiao, Y.; Qiao, S. Z. Charge state manipulation of cobalt selenide catalyst for overall seawater electrolysis. *Adv. Energy Mater*. **2018**, *8*, 1801926.

[22] Jin, H. Y.; Liu, X.; Vasileff, A.; Jiao, Y.; Zhao, Y. Q.; Zheng, Y.; Qiao, S. Z. Single-crystal nitrogen-rich two-dimensional Mo$_5$N$_6$ nanosheets

for efficient and stable seawater splitting. *ACS Nano* **2018**, *12*, 12761–12769.

[23] Kato, Z.; Sato, M.; Sasaki, Y.; Izumiya, K.; Kumagai, N.; Hashimoto, K. Electrochemical characterization of degradation of oxygen evolution anode for seawater electrolysis. *Electrochim. Acta* **2014**, *116*, 152–157.

[24] Juodkazytė, J.; Šebeka, B.; Savickaja, I.; Petrulevičienė, M.; Butkutė, S.; Jasulaitienė, V.; Selskis, A.; Ramanauskas, R. Electrolytic splitting of saline water: Durable nickel oxide anode for selective oxygen evolution. *Int. J. Hydrogen Energy* **2019**, *44*, 5929–5939.

[25] Yu, L.; Zhu, Q.; Song, S. W.; McElhenny, B.; Wang, D. Z.; Wu, C. Z.; Qin, Z. J.; Bao, J. M.; Yu, Y.; Chen, S. et al. Non-noble metal-nitride based electrocatalysts for high-performance alkaline seawater electrolysis. *Nat. Commun.* **2019**, *10*, 5106.

[26] Huang, W. H.; Lin, C. Y. Iron phosphate modified calcium iron oxide as an efficient and robust catalyst in electrocatalyzing oxygen evolution from seawater. *Faraday Discuss.* **2019**, *215*, 205–215.

[27] Zhao, Y. Q.; Jin, B.; Vasileff, A.; Jiao, Y.; Qiao, S. Z. Interfacial nickel nitride/sulfide as a bifunctional electrode for highly efficient overall water/seawater electrolysis. *J. Mater. Chem. A* **2019**, *7*, 8117–8121.

[28] Song, H. J.; Yoon, H.; Ju, B.; Lee, D. Y.; Kim, D. W. Electrocatalytic selective oxygen evolution of carbon-coated $Na_2Co_{1-x}Fe_xP_2O_7$ nanoparticles for alkaline seawater electrolysis. *ACS Catal.* **2020**, *10*, 702–709.

[29] Feng, J. X.; Xu, H.; Dong, Y. T.; Ye, S. H.; Tong, Y. X.; Li, G. R. FeOOH/Co/FeOOH hybrid nanotube arrays as high-performance electrocatalysts for the oxygen evolution reaction. *Angew. Chem., Int. Ed.* **2016**, *55*, 3694–3698.

[30] Yuan, T. B.; Hu, Z.; Zhao, Y. X.; Fang, J. J.; Lv, J.; Zhang, Q. H.; Zhuang, Z. B.; Gu, L.; Hu, S. Two-dimensional amorphous SnO_x from liquid metal: Mass production, phase transfer, and electrocatalytic CO_2 reduction toward formic acid. *Nano Lett.* **2020**, *20*, 2916–2922.

[31] Feng, L. L.; Yu, G. T.; Wu, Y. Y.; Li, G. D.; Li, H.; Sun, Y. H.; Asefa, T.; Chen, W.; Zou. X. X. High-index faceted Ni_3S_2 nanosheet arrays as highly active and ultrastable electrocatalysts for water splitting. *J. Am. Chem. Soc.* **2015**, *137*, 14023–14026.

[32] Lu, X. Y.; Zhao, C. Electrodeposition of hierarchically structured three-dimensional nickel-iron electrodes for efficient oxygen evolution at high current densities. *Nat. Commun.* **2015**, *6*, 6616.

[33] Chen, M. X.; Lu, S. L.; Fu, X. Z.; Luo, J. L. Core-shell structured NiFeSn@NiFe (oxy)hydroxide nanospheres from an electrochemical strategy for electrocatalytic oxygen evolution reaction. *Adv. Sci.* **2020**, *7*, 1903777.

[34] Fang, M.; Han, D.; Xu, W. B.; Shen, Y.; Lu, Y. M.; Cao, P. J.; Han, S.; Xu, W. Y.; Zhu, D. L.; Liu, W. J. et al. Surface-guided formation of amorphous mixed-metal oxyhydroxides on ultrathin MnO_2 nanosheet arrays for efficient electrocatalytic oxygen evolution. *Adv. Energy Mater.* **2020**, *10*, 2001059.

[35] Cui, B. H.; Zhang, M.; Zhao, Y. X.; Hu, S. Heterogenization of few-layer MoS_2 with highly crystalline 3D Ni_3S_2 nanoframes effectively synergizes the electrocatalytic hydrogen generation in alkaline medium. *Mater. Today Energy* **2019**, *13*, 85–92.

[36] Bantignies, J. L.; Deabate, S.; Righi, A.; Rols, S.; Hermet, P.; Sauvajol, J. L.; Henn, F. New insight into the vibrational behavior of nickel hydroxide and oxyhydroxide using inelastic neutron scattering, far/mid-infrared and Raman spectroscopies. *J. Phys. Chem. C* **2008**, *112*, 2193–2201.

[37] Zong, L. B.; Chen, X.; Dou, S. M.; Fan, K. C.; Wang, Z. M.; Zhang, W. J.; Du, Y. M.; Xu, J.; Jia, X. F.; Zhang, Q. et al. Stable confinement of Fe/Fe_3C in Fe, N-codoped carbon nanotube towards robust zinc-air batteries. *Chin. Chem. Lett.*, in press, DOI: 10.1016/j.cclet.2020.08.029.

[38] Liang, H. F.; Gandi, A. N.; Xia, C.; Hedhili, M. N.; Anjum, D. H.; Schwingenschlögl, U.; Alshareef, H. N. Amorphous NiFe-OH/NiFeP electrocatalyst fabricated at low temperature for water oxidation applications. *ACS Energy Lett.* **2017**, *2*, 1035–1042.

[39] Liu, C.; Chen, Z. L.; Rao, D. W.; Zhang, J. F.; Liu, Y. W.; Chen, Y. N.; Deng, Y. D.; Hu, W. B. Behavior of gold-enhanced electrocatalytic performance of NiPtAu hollow nanocrystals for alkaline methanol oxidation. *Sci. China Mater.* **2020**, in press, DOI: 10.1007/s40843-020-1460-y.

[40] Li, J. W.; Lian, R. Q.; Wang, J. Y.; He, S.; Jiang, S. P.; Rui, Z. B. Oxygen vacancy defects modulated electrocatalytic activity of iron-nickel layered double hydroxide on Ni foam as highly active electrodes for oxygen evolution reaction. *Electrochim. Acta* **2020**, *331*, 135395.

[41] Chen, F. S.; Liu, C.; Cui, B. H.; Dou, S. M.; Xu, J.; Liu, S. L.; Zhang, H.; Deng, Y. D.; Chen, Y. N.; Hu, W. B. Regulated synthesis of eutectic Ni_3S_2/NiS nanorods for quasi-solid-state hybrid supercapacitors with high energy density. *J. Power Sources*, **2021**, *482*, 228910.

[42] Yang, Z. B.; Liang, X. Self-magnetic-attracted $Ni_xFe_{(1-x)}$@$Ni_xFe_{(1-x)}O$ nanoparticles on nickel foam as highly active and stable electrocatalysts towards alkaline oxygen evolution reaction. *Nano Res.* **2020**, *13*, 461–466.

[43] Liu, G.; Gao, X. S.; Wang, K. F.; He, D. Y.; Li, J. P. Mesoporous nickel-iron binary oxide nanorods for efficient electrocatalytic water oxidation. *Nano Res.* **2017**, *10*, 2096–2105.

[44] Friebel, D.; Louie, M. W.; Bajdich, M.; Sanwald, K. E.; Cai, Y.; Wise, A. M.; Cheng, M. J.; Sokaras, D.; Weng, T. C.; Alonso-Mori, R. et al. Identification of highly active Fe sites in (Ni,Fe)OOH for electrocatalytic water splitting. *J. Am. Chem. Soc.* **2015**, *137*, 1305–1313.

[45] Lee, S.; Bai, L. C.; Hu. X. L. Deciphering iron-dependent activity in oxygen evolution catalyzed by nickel-iron layered double hydroxide. *Angew. Chem.* **2020**, *132*, 8149–8154.

[46] Bates, M. K.; Jia, Q. Y.; Doan, H.; Liang, W. T.; Mukerjee, S. Charge-transfer effects in Ni-Fe and Ni-Fe-Co mixed-metal oxides for the alkaline oxygen evolution reaction. *ACS Catal.* **2016**, *6*, 155–161.

[47] Zhuang, L. Z.; Jia, Y.; He, T. W.; Du, A. J.; Yan, X. C.; Ge, L.; Zhu, Z. H.; Yao, X. D. Tuning oxygen vacancies in two-dimensional iron-cobalt oxide nanosheets through hydrogenation for enhanced oxygen evolution activity. *Nano Res.*, **2018**, *11*, 3509–3518.

[48] Xie, Q. X.; Cai, Z.; Li, P. S.; Zhou, D. J.; Bi, Y. M.; Xiong, X. Y.; Hu, E. Y.; Li, Y. P.; Kuang, Y.; Sun, X. M. Layered double hydroxides with atomic-scale defects for superior electrocatalysis. *Nano Res.* **2018**, *11*, 4524–4534.

[49] Görlin, M.; de Araujo, J. F.; Schmies, H.; Bernsmeier, D.; Dresp, S.; Gliech, M.; Jusys, Z.; Chernev, P.; Kraehnert, R.; Dau, H. et al. Tracking catalyst redox states and reaction dynamics in Ni-Fe oxyhydroxide oxygen evolution reaction electrocatalysts: The role of catalyst support and electrolyte pH. *J. Am. Chem. Soc.* **2017**, *139*, 2070–2082.

[50] Jin, Y. S.; Huang, S. L.; Yue, X.; Du, H. Y.; Shen, P. K. Mo- and Fe-modified $Ni(OH)_2$/NiOOH nanosheets as highly active and stable electrocatalysts for oxygen evolution reaction. *ACS Catal.* **2018**, *8*, 2359–2363.

[51] Zhang, J. F.; Liu, J. Y.; Xi, L. F.; Yu, Y. F.; Chen, N.; Sun, S. H.; Wang, W. C.; Lange, K. M.; Zhang, B. Single-atom Au/NiFe layered double hydroxide electrocatalyst: Probing the origin of activity for oxygen evolution reaction. *J. Am. Chem. Soc.* **2018**, *140*, 3876–3879.

[52] Hsu, S. H.; Miao, J. W.; Zhang, L. P.; Gao, J. J.; Wang, H. M.; Tao, H. B.; Hung, S. F.; Vasileff, A.; Qiao, S. Z.; Liu, B. An earth-abundant catalyst-based seawater photoelectrolysis system with 17.9% solar-to-hydrogen efficiency. *Adv. Mater.* **2018**, *30*, 1707261.